

This document is confidential and is proprietary to the American Chemical Society and its authors. Do not copy or disclose without written permission. If you have received this item in error, notify the sender and delete all copies.

Wide-field mid-infrared hyperspectral imaging by snapshot phase contrast measurement of optothermal excitation

Journal:	<i>Analytical Chemistry</i>
Manuscript ID	ac-2021-02805u.R1
Manuscript Type:	Article
Date Submitted by the Author:	28-Sep-2021
Complete List of Authors:	Yuan, Tao; Technical University of Munich, School of Medicine Pleitez, Miguel A.; Helmholtz Center Munich German Research Center for Environmental Health, Gasparin, Francesca; Technische Universitat Munchen, Chair of Biological Imaging Ntziachristos, Vasilis; Technical University of Munich, Chair of Biological Imaging

SCHOLARONE™
Manuscripts

Wide-field mid-infrared hyperspectral imaging by snapshot phase contrast measurement of optothermal excitation

Tao Yuan,^{1,2,†} Miguel A. Pleitez,^{1,2,†,*} Francesca Gasparin,^{1,2} Vasilis Ntziachristos^{1,2,*}

¹Technical University of Munich, School of Medicine, Center for Translational Cancer Research (TranslaTUM), Chair of Biological Imaging, D-81675, Munich, Germany

²Helmholtz Zentrum München (GmbH), Institute of Biological and Medical Imaging, D-85764, Neuherberg, Germany

[†]These authors contributed equally to this work

* Corresponding author. Email: bioimaging.translatum@tum.de

Abstract: Vibrational microscopy methods based on Raman scattering or infrared absorption provide a label-free approach for chemical-contrast imaging, but employ point-by-point scanning and impose a compromise between imaging speed and field-of-view (FOV). Optothermal microscopy has been proposed as a promising imaging modality to avoid this compromise, although at restrictively small FOVs capable of imaging only few cells. Here, we present Wide-field Optothermal Mid-infrared Microscopy (WOMiM) for wide-field chemical-contrast imaging based on snapshot pump-probe detection of optothermal signal, by using a custom-made Condenser-free Phase Contrast Microscopy (CPCM) to capture the phase change of samples after mid-infrared (MIR) irradiation. We achieved chemical-contrast for FOVs up to 180 μm in diameter, yielding 10-fold larger imaging areas than the state-of-the-art, at imaging speeds of 1 ms/frame. The maximum possible imaging speed of WOMiM was determined by the relaxation time of optothermal heat, measured to be 32.8 μs in water, corresponding to a frame rate of ~ 30 kHz. This proof-of-concept demonstrates that vibrational imaging can be achieved at unprecedented imaging speed and large FOV, with the potential to significantly facilitate label-free imaging of cellular dynamics.

1. Introduction

Live-cell chemical-contrast microscopy based on vibrational excitation of biomolecules can reveal cell metabolism dynamics in a label-free manner and includes coherent anti-Stokes Raman scattering (CARS) microscopy, stimulated Raman scattering (SRS) microscopy, and (recently) mid-infrared optoacoustic microscopy (MiROM).¹⁻³ However, these modalities rely mainly on image acquisition via point-by-point raster scanning⁴⁻⁶ which imposes a compromise between imaging speed and field-of-view (FOV). In particular, the raster scanning method is not suitable for imaging fast dynamic changes, such as lipid droplets movement along microtubules with velocities ranging in the $\mu\text{m/s}$,⁷⁻⁹ or action potentials in neurons which occur in the range of milliseconds.¹⁰ This is especially limiting when imaging big cells (for example, adipocytes can be up to 100 μm in size¹¹) or large cell populations (hundreds to thousands of cells) needed to obtain statistically relevant analysis. A strategy to increase imaging speed at large FOVs has been to increase the scanning step size (for instance 5 – 20 μm), however this practice notably reduces the overall imaging resolution. For hyperspectral imaging (i.e. imaging at multiple wavelengths), low imaging speed imposes a compromise between FOV and spectral coverage; i.e., the bigger the scanning FOV, the smaller the wavelength range that can be covered within a given time. Additionally, although galvo scanners enable an imaging speed of up to 30 frames/s, they suffer from imaging distortion in large FOVs as the scanning beam

1
2
3
4
5 shifts away from the optical axis. Therefore, there is a need for alternative methods to achieve
6 high-speed chemical-contrast imaging of fast and dynamic cellular changes for large FOVs,
7 wide spectral range, and at high spatial resolution.

8 To avoid the compromise between imaging speed, FOV, spectral coverage, and resolution,
9 various wide-field vibrational microscopy methods for high-speed chemical-contrast imaging
10 have recently been proposed.¹²⁻¹⁶ For instance, wide-field CARS, where a vibrational image is
11 obtained by expanding Stokes and pump beam, achieved video-rate imaging using spectral
12 coverage of four excitation wavelengths.¹² Similarly, quantitative optothermal microscopy,
13 where optothermally induced phase changes are quantitatively measured for chemical-contrast
14 imaging, have achieved imaging speeds up to 10 ms/frame (before averaging) for imaging of
15 intracellular structures, such as nuclei and lipid droplets.^{13, 15} However, both wide-field CARS
16 and quantitative optothermal microscopy are limited to small chemical-contrast FOVs of 10-
17 50 μm (FOVs refer to the diameter of the excitation area), while FOVs above 100 μm are
18 necessary for imaging cell populations or big cells. Quantitative measurements of phase
19 changes usually rely on complex optics that are susceptible to vibration, making it challenging
20 for detecting the subtle phase change after expansion of the Mid-Infrared (MIR) excitation area
21 (due to lower flux density). A recent MIR microscopy method based on a nonlinear
22 interferometer was proposed as a large FOV imaging modality, demonstrating an up to 1.2 mm
23 FOV for the imaging of paraffin-embedded tissue slices at a single MIR wavelength.¹⁶ The
24 function of a nonlinear interferometer relies on Spontaneous Parametric Down-Conversion
25 (SPDC) of a nonlinear crystal. Here, a pump photon is converted into two low energy photons
26 (an idler photon and a signal photon), where the idler photons are used to probe the sample and
27 the signal photons are detected by a camera.¹⁷⁻¹⁹ However, the conversion efficiency of SPDC
28 is typically low, as only a limited number of signal photons reach the detector, resulting in a
29 low signal-to-noise-ratio (SNR).

30 We hypothesized that chemical-contrast imaging at large FOVs and high-speeds can be
31 achieved by probing the phase contrast change using a custom-made Condenser-free Phase
32 Contrast Microscope (CPCM).^{20, 21} In particular, a sample is first imaged by CPCM (MIR-OFF)
33 and subsequently imaged in the same way under MIR irradiation (MIR-ON). Chemical-contrast
34 micrographs are obtained by the difference in MIR-OFF/MIR-ON phase contrast images. Here,
35 acquisition of chemical-contrast images no longer relies on point-by-point raster scanning, and
36 the FOV is determined by the size of the MIR excited area as well as by the imaging area of
37 the phase-contrast microscope.

38 To this end, we introduce Wide-field Optothermal Mid-infrared Microscopy (WOMiM),
39 which uses MIR beams to selectively induce refractive index changes on samples due to the
40 optothermal effect (i.e. heat deposition due to optical absorption). Localized and selective
41 refractive index changes were probed by CPCM. Benefiting from the robustness of CPCM, we
42 were able to detect the phase difference after extending the MIR excitation area up to 180 μm
43 in diameter, which translates to an imaging area approximately 36 times larger than with wide-
44 field CARS microscopies (FOV $\sim 30 \mu\text{m}$),^{12, 22} and 10 times larger than the recent quantitative
45 wide-field optothermal microscopies (FOV $\sim 50 \mu\text{m}$).^{13, 15} By means of WOMiM, we were able
46 to obtain wide-field chemical-contrast images (for a FOV of ca. 180 μm) of triglyceride (TAG)
47 drops in water within 1 ms, which is ~ 20 times faster than point-by-point scanning methods
48 using galvo-resonant scanners with a comparable FOV of 180 μm , and 10 times faster than
49 other recently reported quantitative optothermal microscopy modalities even at a smaller FOV
50 of 50 μm .^{13, 15} Collectively, we demonstrate a proof-of-concept of the proposed method by high-
51 speed chemical-contrast imaging of TAG drops and water, paving the way towards real-time
52 monitoring of cellular dynamics.

53 **2. Experimental section**

54 **2.1 Experimental setup**

1
2
3
4
5 A 9 ns-pulse-width mid-infrared (MIR) Optical Parametric Oscillator (OPO) laser (NT277,
6 EKSPLA; 1 kHz pulse repetition rate) was used as the MIR pump source. The output of OPO
7 laser was then passed through a Germanium window and a MIR polarizer, for the purpose of
8 filtering out the visible signal beam generated by the parametric process and adjusting the MIR
9 irradiation power. The MIR (idler beam) was then focused by a low numerical aperture (NA)
10 gold parabolic mirror (#37248, Edmund Optics, Ltd.; NA = 0.062) on the sample, creating a
11 focus spot of 186.2 μm in diameter (at 3480 cm^{-1}). A custom-made petri-dish with a ZnS
12 window (4ZNS F2505, Crystal GmbH) on the bottom was used to hold the samples. The change
13 of phase due to MIR absorption was probed by a custom-made Condenser-free Phase Contrast
14 Microscope (CPCM), in which an annular illuminator (Aura, Cairn Research, Ltd.) was used
15 for phase illumination to facilitate the MIR irradiation. The annular illuminator was placed
16 below a phase objective (20 \times , Nikon; NA = 0.4) in a conjugate plane of the objective phase
17 ring to fulfil the condition for phase contrast imaging. A high-speed camera (PCO.dimax cs4,
18 PCO AG) was used on the microscope to acquire the phase images (MIR-ON/MIR-OFF). Both
19 the camera and OPO laser were externally triggered by a programmable microcontroller
20 (MSP430, Texas Instruments Inc.). The camera, OPO laser and microcontroller were connected
21 to the computer and the whole system can be operated by a custom-made MATLAB user
22 interface.

23 2.2 Sample preparation

24 Using a 10 mg/ml solution of 1,2-dioleoyl-3-palmitoyl-rac-glycerol (Sigma-Aldrich, Inc.),
25 triglyceride (TAG) drops were prepared by dissolving 1 mg of this solution in 100 μL of a
26 chloroform-methanol solution (2:1). 10 μL of the TAG solution were plated on a custom-made
27 petri-dish with ZnS window, and let dry at room temperature until complete evaporation of
28 chloroform-methanol, leaving the TAG drops on the surface of a ZnS window. The TAG drops
29 sample were then used for proof-of-concept measurements as shown in Figure 1. Water-
30 immersed TAG drops [Figure 2(j-m)] were prepared by adding a 1 mm layer of deionized water,
31 and covered with cover glass (0.17 mm thick) to reduce water evaporation and maintain the
32 thickness of the water layer. Optothermal signal characterization [Figure 2(b-i)] was performed
33 in a layer of 1 mm of water, detecting the signal from water between the ZnS and cover glass.

34 2.3 Image acquisition settings

35 In proof-of-concept measurements [Figure 1(c-f)] or characterization of linearity [Figure
36 1(i-n)], MIR-ON/MIR-OFF phase contrast images were acquired by a monochromatic CMOS
37 camera (FL3-U3-20E4M-C, FLIR Systems, Inc.). Using on-off-level synchronization, the
38 MIR-ON phase images were captured 4 s after OPO switch-on, and MIR-OFF phase images
39 were captured 4 s after OPO switch-off. Both the exposure time of MIR-ON and MIR-OFF
40 phase images were set to 250 ms. To acquire MIR-ON images for the TAG drops, the OPO was
41 tuned to the CH symmetry stretch vibration peak of 2850 cm^{-1} in wavenumber,²³ with excitation
42 flux density of 0.64 $\mu\text{W}/\mu\text{m}^2$ on the sample.

43 A high-speed camera (PCO.dimax cs4, PCO AG) was used for the characterization of the
44 optothermal process [Figure 1(p-r) for TAG drops and Figure 2(b-g) for water] and
45 hyperspectral imaging measurement [Figure 2(j-l)]. Both the characterization of water
46 optothermal process [Figure 2(b-g)] and hyperspectral imaging [Figure 2(j-m)] applied single-
47 pulse-level synchronization, in which MIR-ON and MIR-OFF images were captured at a frame
48 rate of 1 kHz, with an exposure time of 5.5 μs . During characterization of the water optothermal
49 process, the OPO was tuned to a high absorption wavelength of water (3480 cm^{-1} in
50 wavenumber), with excitation flux density of 1.64 $\mu\text{W}/\mu\text{m}^2$ on sample. A subtraction-image
51 was obtained by subtracting the average of 50 MIR-ON images from the average of 50 MIR-
52 OFF phase images. To scan the whole process of optothermal signal, the exposure delay of
53 MIR-ON images was set to a particular sequence (start: 9 μs ; step: 8.2 μs ; stop: 993 μs),
54 resulting 121 subtraction-images. In hyperspectral imaging, the exposure delay was fixed to a
55 value (194.0 μs) that yielded the maximum optothermal signal. The wavenumber of the OPO
56
57
58
59
60

1
2
3
4
5 was tuned from 2830 cm^{-1} to 2950 cm^{-1} , with a step size of 10 cm^{-1} . Average of 18 MIR-ON
6 phase images and 18 MIR-OFF phase images were used for obtaining a subtraction-image.

7 **2.4 Data processing**

8
9 ImageJ was used for calculating subtraction-images and extracting line profiles in the proof-of-
10 concept measurement [Figure 1(e-f) and Figure 1(i-n)]. MATLAB was used to perform
11 exponential fit of the optothermal process of TAG drops, plotting the profile and spectra figures.
12 For hyperspectral imaging, a graphical user interface (GUI) based on MATLAB App Designer
13 was developed for OPO wavelength tuning, synchronization setting, images acquisition and
14 other options. A Gaussian smooth (radius = 2) was applied in Figure 2(b-g) and Figure 2(j-l) to
15 remove the camera hot pixels and dark current noise. Cubic spline interpolation was applied to
16 the WOMiM spectra in Figure 2(n).

17 **3. Results**

18 **3.1 Imaging principle and proof-of-concept**

19
20
21
22
23
24
25
26
27
28
29
30
31
32
33
34
35
36
37
38
39
40
41
42
43
44
45
46
47
48
49
50
51
52
53
54
55
56
57
58
59
60

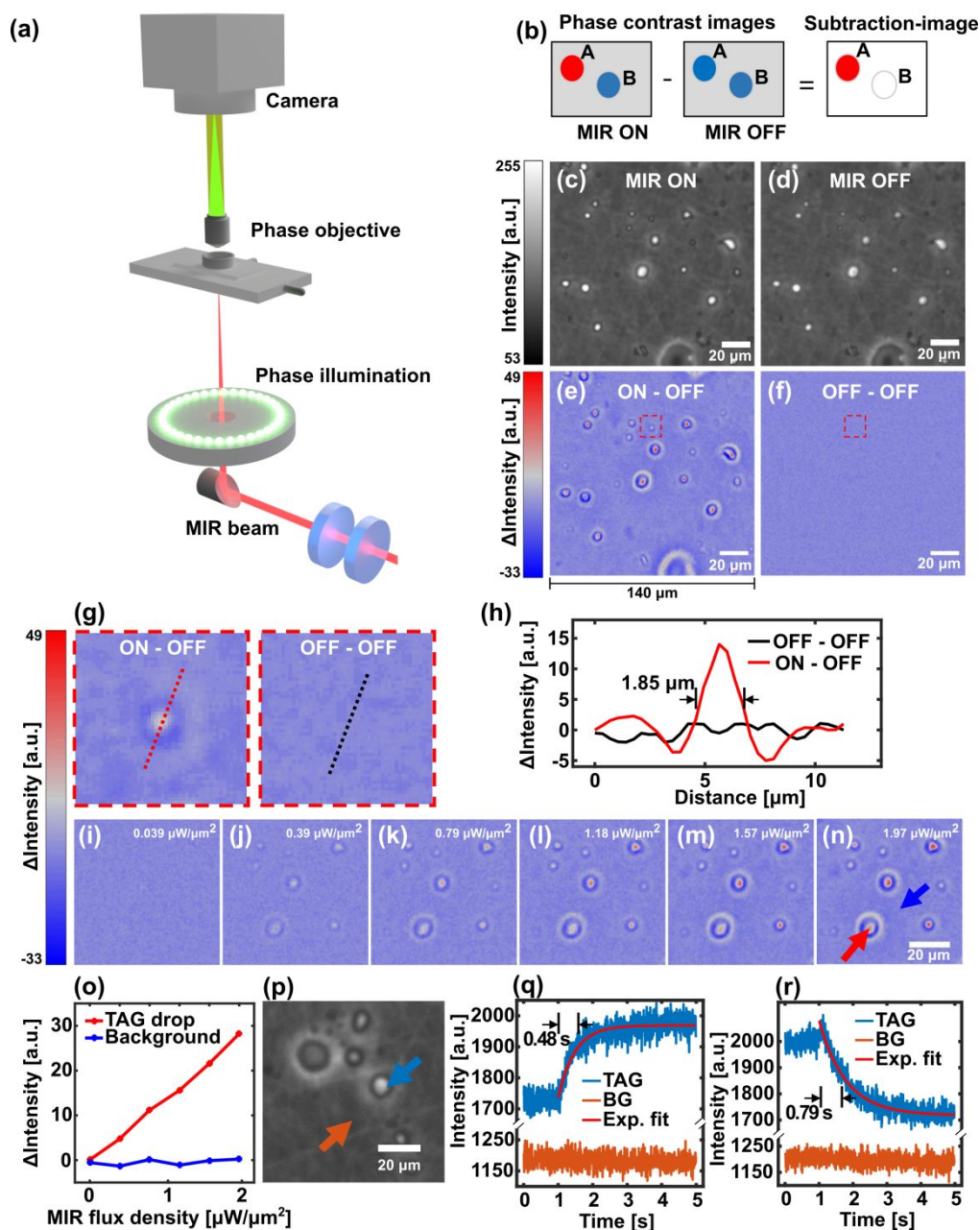


Figure 1. Operational principle and characterization of Wide-field Optothermal Mid-infrared Microscopy (WOMiM). (a) Schematic of WOMiM. MIR pulses are focused on the sample by a parabolic mirror. The phase change due to MIR absorption is obtained by capturing MIR-ON and MIR-OFF micrographs with a condenser-free phase contrast microscope. (b) A chemical-contrast image is obtained by subtracting a MIR-OFF image from a MIR-ON image. (c) A MIR-ON image (MIR wavenumber at 2850 cm^{-1}) and (d) a MIR-OFF image of triglyceride (TAG) drops. (e) A WOMiM micrograph by subtracting (d) from (c). (f) Subtraction of two MIR-OFF images. (g) Zoom-in FOVs of the smallest observed TAG drop, as marked by the red dash rectangles in (e) and (f). (h) Line profiles of the smallest observed TAG drop in (g). (i-n) Illustration of WOMiM micrographs (subtraction-images) at varying MIR excitation flux density ($0.039 \mu\text{W}/\mu\text{m}^2$ to $1.97 \mu\text{W}/\mu\text{m}^2$). (o) Intensity plot of a TAG drop center and an arbitrary point in the background as indicated by red and blue arrows in (n). (p-r) Intensity variation plots as the MIR was turned on at 1 s (q) and turned off at 1 s (r), where the intensity is acquired at the location of the two arrows in (p).

1
2
3
4
5 Figure 1(a) depicts the schematic representation of WOMiM. In the system, a custom-made
6 Condenser-free Phase Contrast Microscope (CPCM) was used to probe the phase change due
7 to MIR absorption. Phase contrast performance of CPCM has been characterized from both
8 experiment and simulation (see Figure S1). MIR pulses were focused by a low NA parabolic
9 mirror, creating a wide excitation area (ca. 180 μm in diameter) on the sample. The phase
10 images were captured by a high-speed camera, which was synchronized with the MIR pulses
11 by a microcontroller.

12 To characterize WOMiM, we used what we refer to as “on-off-level synchronization”. Here,
13 camera exposure was synchronized to the “on” or “off” state of the OPO: a MIR-ON image
14 was captured when the OPO has been active for 4 seconds, and a MIR-OFF image was captured
15 4 seconds after the OPO has stopped. Exposure time of both the MIR-OFF and MIR-ON image
16 was 250 ms. While the on-off level synchronization limits the speed for chemical-contrast
17 imaging (due to the time interval of 4 s for heat dissipation), it provides a straightforward mean
18 for characterizing and demonstrating the working principle of WOMiM.

19 Figure 1(b) depicts the working principle of WOMiM. Subtracting the MIR-OFF image
20 from the MIR-ON image yields a subtraction image (henceforth referred to as “subtraction-
21 image”) and represents the phase contrast difference after MIR illumination. Here, in a wide
22 FOV (determined by the MIR excitation area) with a high MIR absorption sample “A” and low
23 MIR absorption background “B”, the subtraction-image shows high contrast for “A” and low
24 contrast for “B”.

25 As validation of the working principle of WOMiM, Figure 1(c-e) shows a MIR-ON image
26 (at 2850 cm^{-1}) (c), a MIR-OFF image (d), and a subtraction-image (e) of TAG drops on a ZnS
27 window. We observed that contrast of TAG drops was enhanced in the subtraction-image
28 [Figure 1(e)], while contrast of the background was reduced. Figure 1(f) shows the subtraction-
29 image of two MIR-OFF images, serving as a control experiment to characterize the robustness
30 of CPCM. The standard deviation of all pixel intensity values of Figure 1(f) was calculated to
31 be 1.02; this standard deviation indicates that optical stability of the system is comparable to
32 the unit of intensity of the camera—which can change between 0 and 255 in steps of 1.
33 Moreover, no TAG drops were observed in Figure 1(f), suggesting that contrast of TAG drops
34 in the subtraction-image in (e) was caused specifically by MIR absorption properties of the
35 TAG drops.

36 Figure 1(g) provides zoom-in views of the smallest observed TAG drop from Figure 1(e)
37 and Figure 1(f) (red dashed rectangles). Figure 1(h) shows the contrast profiles of red and black
38 dashed lines in (g), used to characterize the resolution and the noise of WOMiM. Full-Width-
39 at-Half-Maximum (FWHM) of this TAG drop profile was 1.85 μm . This value is close to the
40 Abbe diffraction limit of 1.75 μm in the case when using a high NA mid-infrared objective
41 ($d = \lambda/2\text{NA}$, where $\text{NA} = 1$, $\lambda = 3.508 \mu\text{m}$). However, benefiting from the pump-probe detection,
42 our results demonstrate that the diffraction limit resolution can be achieved with low NA optics
43 (i.e., a mid-infrared parabolic mirror with $\text{NA} = 0.062$ and a visible objective with $\text{NA} = 0.4$).

44 Figure 1(i-n) depicts several subtraction-images at different laser power, used to
45 characterize the linearity of WOMiM image contrast with MIR flux density (radiant energy per
46 unit time per unit area). We observed an increase in the contrast of TAG drops as the excitation
47 flux density increased from 0.039 $\mu\text{W}/\mu\text{m}^2$ to 1.97 $\mu\text{W}/\mu\text{m}^2$. Figure 1(o) presents an intensity
48 vs. flux density plot of two locations: the TAG drop center and background, as indicated by red
49 and blue arrows, respectively, in Figure 1(n). The plot shows a linear relation between MIR
50 excitation and intensity of the subtraction-image. Importantly, we noticed that the chemical-
51 contrast is observable at a flux density of 0.39 $\mu\text{W}/\mu\text{m}^2$, which is ~ 5 orders of magnitude
52 lower than the flux density of Raman microscopy (15 $\text{mW}/\mu\text{m}^2$),²⁴ since Raman microscopy focuses
53 light on a small spot to irradiate the sample. This provides a great potential for reducing cellular
54 phototoxicity.

55 Figure 1(p) shows the phase contrast image (MIR-OFF) of a 50 μm FOV, with positions of
56 a TAG drop and background marked by a blue and red arrow, respectively. Figure 1(q) shows
57
58
59
60

an intensity variation plot of the two marked locations with a MIR switch-on time at 1 s; Figure 1(r) is the corresponding plot with a MIR switch-off time at 1 s. The two intensity variation plots were used to characterize the time scale of the heating and cooling process for the purpose of choosing a proper time interval for capturing MIR-ON and MIR-OFF images. Figure 1(q) indicates that the intensity of the TAG drop increased immediately after MIR start, while the background intensity remained stable. Exponential fit of the intensity increase yielded a time constant of 0.48 s for heating, and the exponential fit of the intensity decrease yielded a time constant of 0.79 s for cooling as shown in Figure 1(r). The values of 0.48 s and 0.79 s indicate that the time interval of 4 s chosen in “on-off-level synchronization” was sufficient for ensuring high contrast in MIR-ON images and avoiding residual heat in MIR-OFF.

3.2 Optothermal signal characterization and hyperspectral imaging

We next performed further functional characterization of our system. Figure 2(a) shows a diagram of a trigger pulse train used to obtain optothermal signal in water. As shown in the diagram, “OPO trigger in”, which is generated by a microcontroller, was introduced to the OPO with a frequency of 1 kHz to generate MIR pulses. After a delay (referred to as “exposure delay”), “camera trigger in” triggers the camera to acquire images at a frequency of 1 kHz (MIR-ON images). The camera captured 50 MIR-ON and 50 MIR-OFF images, with both sets of 50 images subsequently averaged to increase the SNR. Finally, the subtraction-image was obtained by subtracting the averaged MIR-OFF image from the averaged MIR-ON image as before. In this configuration, since each single MIR-ON image was captured as a MIR pulse arrived, this synchronization was referred to as “single-pulse-level synchronization” (see Methods). Here, we can adjust “exposure delay” to monitor the generation and the dissipation process of a single pulse optothermal signal.

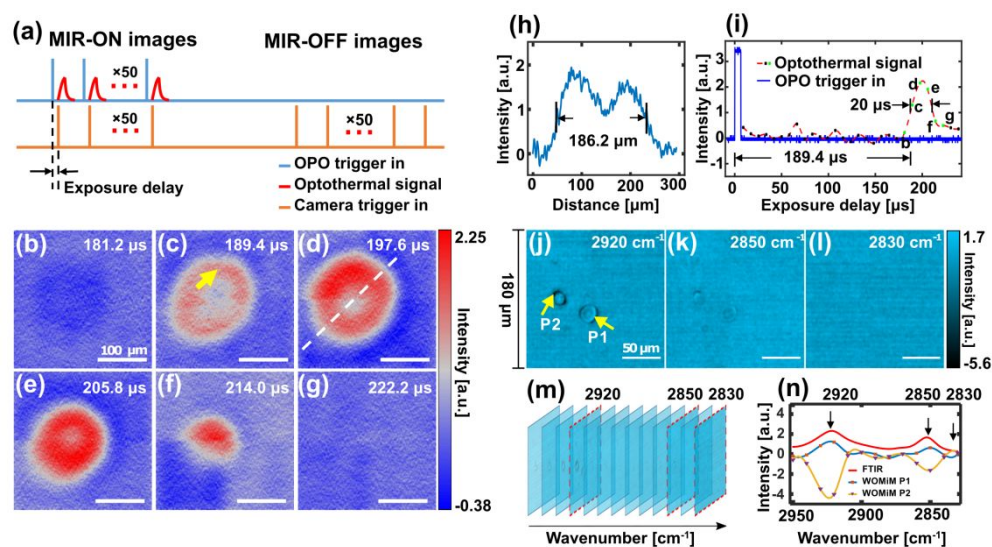


Figure 2. Imaging of optothermal signal in water and hyperspectral imaging of TAG drops. (a) Schematic diagram of a pulse train for single-pulse-level synchronization. In this synchronization mode, each single MIR-ON image is captured as MIR pulse arrive. The corresponding MIR-OFF image is later captured when OPO trigger stop. (b-g) Illustration of subtraction-images with the exposure delay varying from 181.2 μs to 222.2 μs . Each image is a subtraction of 50-averaged MIR-ON and 50-averaged MIR-OFF phase images. (h) Line profile across the 2D optothermal signal (hot spot) for characterization of the MIR excitation area in (d). The line profile suggests a FWHM of 186.2 μm for the diameter of MIR excitation area. (i) Plot of “OPO trigger in” and the optothermal signal, where the optothermal signal is the z-profile of a pixel [indicated in (c)] from an image stack (exposure delay varies from 9 μs to 238.6 μs , with a step size of 8.2 μs). Dots (Black or green): original data from the image stack. Red dashed line: cubic spline interpolation. The green dots in (i) correspond to values from six images in (b-g) as labeled by “b” to “g”. (j-l)

1
2
3
4
5 Three selected images from a hyperspectral image stack. Scale bar 50 μm . (m) The hyperspectral image stack. The
6 wavenumber varies from 2950 cm^{-1} to 2830 cm^{-1} , with a step size of 10 cm^{-1} . (n) WOMiM spectra of selected points,
7 as indicated by the arrows in (j), and the corresponding TAG spectrum measured by FTIR. In the WOMiM spectra,
8 smooth lines are obtained using cubic spline interpolation. In (b-g) and (j-l), dark current noise of camera was filtered
9 out by Gaussian blurry.

10 Because cells are cultured in an aqueous environment, knowing the relaxation time of
11 optothermal heat in water is fundamental, but this critical information has not been previously
12 provided. In order to characterize a single pulse optothermal generation and dissipation in
13 water, six frames with the exposure delay varying from 181.2 μs to 222.2 μs were acquired
14 [Figure 2 (b-g)]. Figure 2(b) depicts a subtraction-image before optothermal contrast
15 generation. The first optothermal contrast image (referred to as “hot spot”) was observed at an
16 exposure delay of 189.4 μs [Figure 2(c)]. Due to the thermal dissipation, the hot spot reduced
17 in size over time [Figure 2(c-f)], and completely disappeared after an exposure delay of 222.2
18 μs [Figure 2(g)], suggesting that optothermal contrast lasts $\sim 32.8 \mu\text{s}$ ($222.2 \mu\text{s} - 189.4 \mu\text{s}$) in
19 water. Figure 2(h) shows a line profile across the hot spot in Figure 2(d), which was used to
20 characterize the diameter of the MIR irradiation area. FWHM of the hot spot line profile
21 indicates that MIR irradiated an area of 186.2 μm in diameter. Since the chemical-contrast of
22 WOMiM was generated from MIR absorption, this irradiation spot size suggests a chemical-
23 contrast FOV of 186.2 μm . To achieve a bigger FOV, one can increase the area of the MIR
24 irradiation spot by vertically shifting the parabolic mirror. We noticed that in Figure 2(c-e), the
25 Gaussian hot spot is flattened in the center, providing a homogenous chemical-contrast FOV.
26 The flattened Gaussian hot spot results from the compensation of a Gaussian excitation spot
27 and doughnut-shaped contrast provided by CPCM, which has been confirmed by its simulation
28 (see Figure S2).

29 Figure 2(i) depicts a plot of intensity vs. time for a pixel as indicated by a yellow arrow in
30 Figure 2(c), which was used to illustrate the optothermal contrast at a longer time scale
31 compared with Figure 2(b-g). The plot was obtained by setting “exposure delay” as a sequence
32 (start: 9 μs ; step: 8.2 μs ; stop: 238.6 μs). The six green dots, labelled by “b” to “g”, present the
33 optothermal signal from Figure 2(b-g). As shown in Figure 2(i), by applying cubic spline
34 interpolation to the optothermal signal, we obtained a FWHM of $\sim 20 \mu\text{s}$. Note that we observed
35 a time delay (189.4 μs) between the trigger pulse of “OPO trigger in” and the optothermal
36 signal, which is due to OPO’s intrinsic electronic delay between “OPO trigger in” and MIR
37 pulse output.

38 Figure 2(j-l) depicts three subtraction-images of TAG drops in water when WOMiM was
39 tuned to 2920 cm^{-1} (j), 2850 cm^{-1} (k) and 2830 cm^{-1} (l), used to validate WOMiM’s chemical-
40 contrast imaging ability. We observed enhanced contrast of TAG drops at 2920 cm^{-1} [Figure
41 2(j)], which is known as a strong TAG absorption peak due to the CH bond asymmetry stretch
42 vibration.²³ We also observed the absorption peak of the TAG drops at 2850 cm^{-1} [Figure 2(k)]
43 assigned to the CH symmetry stretch vibration.²³ Because of weak absorption at 2830 cm^{-1} ,
44 TAG drops showed no contrast at this wavenumber [Figure 2(l)]. The three images obtained
45 from three wavenumbers demonstrated WOMiM’s ability of bond-selective imaging enabled
46 by tuning the OPO to the corresponding bond vibration wavenumber. Note that the three images
47 in Figure 2(j-l) were selected from hyperspectral images stack [Figure 2(m)]. Benefiting from
48 the high imaging speed, the acquisition time for this hyperspectral images stack took
49 approximately 0.26 s. According to “single-pulse-level synchronization”, the actual acquisition
50 time for each chemical-contrast image (with FOV of 180 μm) can go down to 1 ms. In this
51 hyperspectral image stack [Figure 2(m)], we averaged 18 images for each wavelength to
52 increase the SNR.

53 Figure 2(n) shows WOMiM spectra of TAG drops in Figure 2(j-l) and a Fourier Transform
54 infrared (FTIR) spectrum of TAG which was performed as validation. WOMiM spectra were
55 obtained from the z-profile of hyperspectral images (from 2950 cm^{-1} to 2830 cm^{-1} with a step
56
57
58
59
60

of 10 cm^{-1}), with the spectra position indicated by two arrows in Figure 2(j). The spectra obtained from WOMiM and FTIR are in good agreement.

4. Conclusion

Here we presented WOMiM as a novel modality for high-speed chemical-contrast imaging and validated its usability by imaging TAG drops. Chemical-contrast FOVs up to $180 \mu\text{m}$ were achieved, which is an area 36 times bigger than the current state-of-the-art wide-field CARS imaging modality (FOV $\sim 30 \mu\text{m}$ in diameter).^{12, 22} Furthermore, WOMiM can provide chemical-contrast imaging speeds up to 1 ms/frame, which is 3 orders of magnitude faster than mechanical point-by-point scanning methods,³⁻⁶ and 20 times faster than the galvo-resonant scanning method.

Capturing the phase contrast difference induced by MIR absorption for chemical-contrast imaging is a promising novel technique recently proposed,¹³⁻¹⁵ offering unique advantages in imaging speed compared to point-by-point scanning methods. We herein demonstrate for the first time optothermal imaging FOVs of over $180 \mu\text{m}$ by expanding the MIR excitation area while maintaining high imaging speeds (1 ms/frame). Although it seems straightforward for achieving wider FOVs, expanding the MIR excitation area is not trivial because the flux density over the excitation area decreases by the square of the excitation diameter. Similarly, the optothermal signal also decreases by the square of the excitation diameter, which leads to small phase changes. Detecting the subtle change in the phase contrast requires a robust phase readout method, which is met by CPCM. The high imaging speed combined with the large FOV might meet the need for imaging highly dynamic processes in cells.^{7-9, 25, 26} Given the high imaging speed, hyperspectral imaging with broad spectral coverage (13 wavelengths in our case) was obtained in 0.26 s, with the potential of facilitating the identification of spectral fingerprints of specific biomolecules of interest.

According to optothermal signal characterization in Figure 2(b-g), the time interval between a single pulse MIR-ON and MIR-OFF image can be as short as $32.8 \mu\text{s}$, by taking Figure 2(c) as the MIR-ON image and taking Figure 2(g) as the MIR-OFF image. This transit time suggests that WOMiM can theoretically reach a frame rate of 30,488 Hz with a FOV of $180 \mu\text{m}$. To achieve this maximum imaging speed, one could for instance increase the MIR pulse repetition rate to 30,488 Hz. A previous study claimed that 70 kHz can be possible with a relaxation time of $6.9 \mu\text{s}$.¹³ However, even though cells are cultured in a water environment (culture medium), the critical relaxation time of water was not mentioned in this study and the characterization of relaxation time was performed using oil film (or beads in DMSO). We addressed this fundamental gap in the current study. Moreover, we observed a linear relation between MIR excitation power and intensity of optothermal contrast as shown in Figure 1(i-o). The linear relationship provides a way for quantifying the phase change due to MIR absorption. This linearity may be due to the small temperature change in the sample (within 1 degree). Both the thermo-optic coefficient (dn/dT) of water and TAG are stable within such a small temperature variation.^{27, 28}

WOMiM can reduce the trade-off between imaging time and imaging area and achieve hyperspectral imaging in a wide wavelength range. Conventionally, a hyperspectral image cube is obtained by acquiring a complete spectrum for each pixel of the FOV, with the imaging time rapidly increasing as the imaging area expands. For example, hyperspectral imaging of an area with 150×150 points requires 22500 spectra. Given a spectral acquisition time of 0.5 s, the total imaging time for this hyperspectral image cube is 3.125 h,²⁹ which is too long for imaging dynamic processes since the migration speed of cells is around $0.5 \mu\text{m}/\text{min}$.^{30, 31} Using the proposed method, a hyperspectral imaging cube of 350×350 points (FOV of $\sim 180 \mu\text{m}$ in diameter) can be obtained with total imaging time of 0.26 s.

When applied on a chemically homogeneous sample, WOMiM generates optical absorption spectra of the sample at every pixel of the excited FOV (MIR irradiation area). This is because, as the sample absorbs the MIR radiation, localized heat is generated at every location of the

MIR excitation area due to the optothermal effect, resulting in changes of optical path length at every pixel over the area. However, CPCM is known for a “shade-off” artifact when measuring homogeneous samples, with the contrast weaker in the center, i.e., generating spectra of different intensity in the center and edges of the FOV. This “shade-off” artifact is partly compensated by the Gaussian intensity profile of the MIR irradiation (MIR intensity is stronger in the center); additionally, detailed characterization of the phase-contrast reference field can be used for post-processing correction of the measured spectra in homogeneous samples.

Moreover, owing to the high imaging speed up to 1 ms/frame, WOMiM is a potential tool for investigation of intracellular transport, which requires high temporal resolution. For example, lipid droplets are known to undergo a “saltatory” motion, characterized by abrupt movements and changes in direction.²⁵ The saltatory motion of many organelles occurs at speeds of $\mu\text{m/s}$.⁷ Investigations of lipid droplets saltatory motion traditionally rely on lipophilic stains where the imaging acquisition rate is limited by fluorescent signal intensity, with a weaker fluorescent signal requiring longer exposure time for a high SNR.²⁵ WOMiM could benefit two aspects of intracellular transport research: high imaging speeds can ensure precise localization and tracking of organelles while also minimizing blurriness/motion artefacts due to the saltatory motion.

Importantly, similarly to a Zernike phase contrast microscope, the well-known “halo” artefacts were observed in WOMiM. The artefacts can lead to an unexpected peak that may reduce the reliability of the spectrum. However, to minimize this problem, an apodized phase objective or algorithm-based process can be applied.³²⁻³⁴ Regarding to acquisition time, if taking into account the time needed for data transfer from camera to PC and OPO wavelength tuning, ~ 10 minutes is needed for acquiring the whole hyperspectral stack of 13 images. This can be improved by technical optimization, such as using onboard averaging for MIR-ON and MIR-OFF images before transferring to PC.

In summary, this work shows that vibrational imaging can be achieved at unprecedented fast imaging speeds (3 orders of magnitude faster than chemical point-by-point scanning methods, and 20 times faster than galvo scanning methods) in a wide FOV (36 times larger than recently reported wide-field CARS imaging) through the pump-probe detection of optothermal signal, which may meet the important need for hyperspectral imaging of intracellular dynamics in the future.

Funding. The research leading to these results has received funding from the Deutsche Forschungsgemeinschaft (DFG), Germany (Gottfried Wilhelm Leibniz Prize 2013; NT 3/10-1), as well as from the European Research Council (ERC) under the European Union’s Horizon 2020 research and innovation program under grant agreement No 694968 (PREMSOT).

Acknowledgments. We thank Dr. Sergey Sulima with help editing the manuscript. We thank Yuanhui Huang for his suggestions and discussion on the initial version of the manuscript. We thank the China Scholarship Council (CSC) for financially supporting Tao Yuan’s PhD study at the Technical University of Munich.

Supporting information. Characterization of the condenser-free phase contrast microscope (CPCM) by simulation and experimentally (Figure S1). Characterization of the mid-infrared (MIR) irradiation area (Figure S2).

Author contributions. M.A.P. created the imaging concept. T.Y. built the imaging system, which includes synchronization of OPO and camera, automation of hyperspectral imaging, and writing a MATLAB user interface for system control. F.G. prepared the triglyceride droplets and provided the FTIR spectrum. T.Y. performed all the experiments, analyzed the results and visualized the figures. M.A.P. and V.N supervised the whole study. All authors edited the manuscript.

Competing interests. V.N. is an equity owner and consultant at iThera Medical GmbH, member of the Scientific Advisory Board at SurgVision BV / Bracco Sp.A, owner at Spear UG, founder and consultant at I3. V.N. and M.A.P. are founder of sThesis GmbH (i.Gr.).

Data availability. All data are available in the main text or the supplementary materials.

References

- (1) Folick, A.; Min, W.; Wang, M. C., Label-free imaging of lipid dynamics using Coherent Anti-stokes Raman Scattering (CARS) and Stimulated Raman Scattering (SRS) microscopy, *Curr. Opin. Genet. Dev.* **2011**, *21*, 585-590.
- (2) Ji, M.; Orringer, D. A.; Freudiger, C. W.; Ramkissoon, S.; Liu, X.; Lau, D.; Golby, A. J.; Norton, I.; Hayashi, M.; Agar, N. Y., Rapid, label-free detection of brain tumors with stimulated Raman scattering microscopy, *Sci. Transl. Med.* **2013**, *5*, 201ra119-201ra119.
- (3) Pleitez, M. A.; Khan, A. A.; Soldà, A.; Chmyrov, A.; Reber, J.; Gasparin, F.; Seeger, M. R.; Schätz, B.; Herzig, S.; Scheideler, M., Label-free metabolic imaging by mid-infrared optoacoustic microscopy in living cells, *Nat. Biotechnol.* **2019**, 1-4.
- (4) Kee, T. W.; Cicerone, M. T., Simple approach to one-laser, broadband coherent anti-Stokes Raman scattering microscopy, *Opt. Lett.* **2004**, *29*, 2701-2703.
- (5) van Manen, H.-J.; Kraan, Y. M.; Roos, D.; Otto, C., Single-cell Raman and fluorescence microscopy reveal the association of lipid bodies with phagosomes in leukocytes, *Proc. Natl. Acad. Sci.* **2005**, *102*, 10159-10164.
- (6) Lim, S.-H.; Caster, A. G.; Leone, S. R., Single-pulse phase-control interferometric coherent anti-Stokes Raman scattering spectroscopy, *Phys. Rev. A* **2005**, *72*, 041803.
- (7) Shubeita, G. T.; Tran, S. L.; Xu, J.; Vershinin, M.; Cermelli, S.; Cotton, S. L.; Welte, M. A.; Gross, S. P., Consequences of motor copy number on the intracellular transport of kinesin-1-driven lipid droplets, *Cell* **2008**, *135*, 1098-1107.
- (8) Olzmann, J. A.; Carvalho, P., Dynamics and functions of lipid droplets, *Nat. Rev. Mol. Cell Biol.* **2019**, *20*, 137-155.
- (9) Pol, A.; Martin, S.; Fernandez, M. A.; Ferguson, C.; Carozzi, A.; Luetterforst, R.; Enrich, C.; Parton, R. G., Dynamic and regulated association of caveolin with lipid bodies: modulation of lipid body motility and function by a dominant negative mutant, *Mol. Biol. Cell* **2004**, *15*, 99-110.
- (10) Bean, B. P., The action potential in mammalian central neurons, *Nat. Rev. Neurosci.* **2007**, *8*, 451-465.
- (11) Verboven, K.; Wouters, K.; Gaens, K.; Hansen, D.; Bijnen, M.; Wetzels, S.; Stehouwer, C.; Goossens, G.; Schalkwijk, C.; Blaak, E., Abdominal subcutaneous and visceral adipocyte size, lipolysis and inflammation relate to insulin resistance in male obese humans, *Sci. Rep.* **2018**, *8*, 1-8.
- (12) Shen, Y.; Wang, J.; Wang, K.; Sokolov, A. V.; Scully, M. O., Wide-field coherent anti-stokes raman scattering microscopy based on picosecond supercontinuum source, *APL Photonics* **2018**, *3*, 116104.
- (13) Zhang, D.; Lan, L.; Bai, Y.; Majeed, H.; Kandel, M. E.; Popescu, G.; Cheng, J.-X., Bond-selective transient phase imaging via sensing of the infrared photothermal effect, *Light Sci. Appl.* **2019**, *8*, 116.
- (14) Toda, K.; Tamamitsu, M.; Nagashima, Y.; Horisaki, R.; Ideguchi, T., Molecular contrast on phase-contrast microscope, *Sci. Rep.* **2019**, *9*, 9957.
- (15) Tamamitsu, M.; Toda, K.; Shimada, H.; Honda, T.; Takarada, M.; Okabe, K.; Nagashima, Y.; Horisaki, R.; Ideguchi, T., Label-free biochemical quantitative phase imaging with mid-infrared photothermal effect, *Optica* **2020**, *7*, 359-366.
- (16) Kviatkovsky, I.; Chrzanowski, H. M.; Avery, E. G.; Bartolomeaus, H.; Ramelow, S., Microscopy with undetected photons in the mid-infrared, *Sci. Adv.* **2020**, *6*, eabd0264.
- (17) Zou, X.; Wang, L. J.; Mandel, L., Induced coherence and indistinguishability in optical interference, *Phys. Rev. Lett.* **1991**, *67*, 318.
- (18) Lemos, G. B.; Borish, V.; Cole, G. D.; Ramelow, S.; Lapkiewicz, R.; Zeilinger, A., Quantum imaging with undetected photons, *Nature* **2014**, *512*, 409-412.
- (19) Chekhova, M.; Ou, Z., Nonlinear interferometers in quantum optics, *Adv. Opt. Photonics* **2016**, *8*, 104-155.
- (20) Webb, K. F.; de Fillipi, G.; Johnston, N., Condenser-free zernike phase contrast imaging for scanning probe microscopy, *Microsc. Anal.* **2013**, *27*, 27-32.
- (21) Webb, K. F., Condenser - free contrast methods for transmitted - light microscopy, *J. Microsc.* **2015**, *257*, 8-22.
- (22) Duarte, A. S.; Schnedermann, C.; Kukura, P., Wide-field detected fourier transform CARS microscopy, *Sci. Rep.* **2016**, *6*, 37516.
- (23) Coates, J., Interpretation of infrared spectra, a practical approach, *Encyclopedia of analytical chemistry: applications, theory and instrumentation* **2006**.
- (24) Murugkar, S.; Brideau, C.; Ridsdale, A.; Naji, M.; Stys, P. K.; Anis, H., Coherent anti-Stokes Raman scattering microscopy using photonic crystal fiber with two closely lying zero dispersion wavelengths, *Opt. Express* **2007**, *15*, 14028-14037.
- (25) Welte, M. A., Bidirectional transport along microtubules, *Curr. Biol.* **2004**, *14*, R525-R537.
- (26) Welte, M. A., Fat on the move: intracellular motion of lipid droplets, *Biochem. Soc. Trans.* **2009**, *37*, 991-996.
- (27) Gouw, T.; Vlugter, J., Physical properties of triglycerides. I. Density and refractive index, *Fette, Seifen, Anstrichmittel* **1966**, *68*, 544-549.
- (28) Kim, Y. H.; Park, S. J.; Jeon, S.-W.; Ju, S.; Park, C.-S.; Han, W.-T.; Lee, B. H., Thermo-optic coefficient measurement of liquids based on simultaneous temperature and refractive index sensing capability of a two-mode fiber interferometric probe, *Opt. Express* **2012**, *20*, 23744-23754.

- 1
2
3
4
5 (29) Salehi, H.; Derely, L.; Vegh, A.-G.; Durand, J.-C.; Gergely, C.; Larroque, C.; Fauroux, M.-A.; Cuisinier, F. J.,
6 Label-free detection of anticancer drug paclitaxel in living cells by confocal Raman microscopy, *Appl. Phys. Lett.*
7 **2013**, *102*, 113701.
8 (30) Yan, J.; Irimia, D., Stochastic variations of migration speed between cells in clonal populations, *Technology*
9 **2014**, *2*, 185-188.
10 (31) Hui, J.; Pang, S. W., Cell migration on microposts with surface coating and confinement, *Biosci. Rep.* **2019**, *39*.
11 (32) Yin, Z.; Kanade, T.; Chen, M., Understanding the phase contrast optics to restore artifact-free microscopy
12 images for segmentation, *Med. Image Anal.* **2012**, *16*, 1047-1062.
13 (33) Otaki, T., Artifact halo reduction in phase contrast microscopy using apodization, *Opt. Rev.* **2000**, *7*, 119-122.
14 (34) Nguyen, T. H.; Kandel, M.; Shakir, H. M.; Best-Popescu, C.; Arikath, J.; Do, M. N.; Popescu, G., Halo-free
15 phase contrast microscopy, *Sci. Rep.* **2017**, *7*, 44034.
16
17
18
19
20
21
22
23
24
25
26
27
28
29
30
31
32
33
34
35
36
37
38
39
40
41
42
43
44
45
46
47
48
49
50
51
52
53
54
55
56
57
58
59
60

For Table of Contents Only

